Acoustic streaming in the transducer plane in ultrasonic particle manipulation devices†

Junjun Lei, Peter Glynne-Jones* and Martyn Hill

Faculty of Engineering and the Environment, University of Southampton, Southampton, UK
*P.Glynne-Jones@soton.ac.uk

†Electronic Supplementary Information (ESI) is available. "simulation of particle trajectories.mht" shows a 3D animation of the simulated particle trajectories and "PIV measurement of particle motion.avi" is a video of the four quadrant streaming observed experimentally.

In acoustofluidic manipulation and sorting devices, Rayleigh streaming flows are typically found in addition to the acoustic radiation forces. However, experimental work from various groups has described acoustic streaming that occurs in planar devices in a plane parallel to the transducer face. This is typically a four-quadrant streaming pattern with the circulation parallel to the transducer. Understanding its origins is essential for creating designs that limit or control this phenomenon. The cause of this kind of streaming pattern has not been previously explained as it is different from the well-known classical streaming patterns such as Rayleigh streaming and Eckart streaming, whose circulation planes are generally perpendicular to the face of the acoustic transducer. In order to gain insight into these patterns we present a numerical method based on Nyborg's limiting velocity boundary condition that includes terms ignored in the Rayleigh analysis, and verify its predictions against experimental PIV results in a simple device. The results show that the modelled particle trajectories match those found experimentally. Analysis of the dominant terms in the driving equations shows that the origin of this kind of streaming pattern is related to the circulation of the acoustic intensity.

I. Introduction

Particle manipulation using acoustic radiation forces from ultrasonic standing waves, recently reviewed in *Review of Modern Physics*[1] and *Lab on a Chip*[2], has gained increased attention in recent years and is recognised as being well-suited to particle handling in microfluidic channels as it is non-invasive and requires no pre-treatment of the particles regardless of their optical or charge properties. When an ultrasonic standing wave field is established in a microfluidic channel, the particles suspended in the fluid experience two main forces: acoustic radiation forces (ARF) from their interaction with the sound field; and acoustic streaming induced drag forces (ASF). Previous experimental work on acoutophoresis has shown both ARF-dominated motion and ASF-dominated motion. Typically, in a low MHz field the motion of particles of diameters larger than about 2 μm is dominated by the ARF. Recent experimental work[3-5] has shown excellent agreement with theoretical predictions based on well-established theory[6, 7]. However, during the process of particle manipulation, acoustic streaming can disrupt the manipulation of particles with diameter smaller than 2 μm. As Spengler *et al.*[8] demonstrated, streaming currents can significantly influence the manipulation because the convective drag, generated by acoustic streaming can be comparable to the lateral direct radiation force in the nodal plane. Kuznetsova and Coakley[9] later investigated the roles of acoustic streaming on microparticle concentration and found that 1 μm particles in a half wavelength resonator were convected by streaming from the centre to the edge of the chamber thus undermining the concentration process.

In microfluidic ultrasonic particle manipulation devices, the acoustic streaming field is generally dominated by boundary-driven streaming (Eckart streaming requires acoustic absorption over longer distances than those typically found in such devices[10]). Boundary streaming is a result of the interaction between the acoustic oscillation and solid boundaries. Rayleigh[11] was the first to present a theoretical analysis of a boundary layer driven acoustic streaming field. With a series of assumptions, he obtained equations for the steady motion of periodic vortices within a standing wave field, comprising four pairs of counter-rotating vortices within each wavelength. His solution only describes the fluid motion outside the viscous boundary layer, so it is commonly referred to as 'outer streaming' as well as 'Rayleigh streaming'. Subsequently, a series of modifications of Rayleigh's solution have been proposed, most notably by Westervelt[12], Nyborg[13] and Schlichting[14], reviewed by Boluriaan *et al.*[15] and Wiklund *et al.*[16]. Hamilton *et al.*[17] derived an analytical solution for the acoustic streaming generated by a standing wave confined by parallel plates that described the streaming field inside the viscous boundary layer in addition to the outer streaming field. These theoretical analyses have been complemented by experimental work in acoustofluidic systems and numerical simulations. The acoustic streaming in a standing wave field in an air-filled closed duct was simulated by Kawahashi and Arakawa[18] by applying a fourth-order spatial difference method and by Aktas and Farouk[19] using a flux-corrected transport algorithm. They directly solved the compressible Navier-Stokes equations using a control-volume-based finite-volume method based on the flux-corrected transport (FCT) algorithm. The classical Rayleigh streaming field in a cylindrical tube was numerically simulated by Sastrapradja and Sparrow[20] using the vorticity transport equation (VTE). Recently, Rayleigh streaming in a silicon-glass chip was modelled by Muller *et al.*[21]. Simulations showing the transition of acoustophoretic motion from that dominated by ASF to that dominated by ARF were numerically studied.

The literature discussed above generally describe cases in which the plane of the streaming vortices contains the axis of the standing or travelling waves (in most cases this axis is perpendicular to the transducer). However experimental observations in planar microfluidic resonators have described streaming patterns with vortices flowing parallel to the transducer plane[16, 22]. Similar vortices had previously been described by Spengler *et al.*[23] and later work from Kuznetsova and Coakley[9] also discusses 'unexpected wall-independent' suspension vortices with circulation planes parallel to the transducer radiating surface. They called this streaming pattern an "unexpected vortex" for the reason that this kind of streaming pattern is different from the classical streaming (*e.g.* Rayleigh streaming[11] and Eckart streaming[24]) whose vortex plane contains the axis of the standing or travelling waves. In real standing wave devices there are also acoustic energy gradients in the lateral directions perpendicular to the standing wave axis. In many cases these are insignificant in comparison with the axial gradients, but they become more significant in planar resonators with large surface areas[25]. This paper investigates whether these lateral energy gradients may be the cause of some of the unexpected streaming patterns observed in planar microfluidic resonators.

Despite having been observed experimentally for more than a decade, the mechanism underlying this kind of streaming pattern has not been fully investigated. In this paper, we present a steady, four-quadrant, symmetric streaming pattern with the circulation plane parallel to the transducer plane, which has frequently been observed in our ultrasonic particle manipulation devices and is similar to that described by Hammarstrom *et al.*[22]. A Finite element method is used to numerically simulate the streaming field and particle trajectories in relevant devices in order to understand the mechanism of this type of streaming pattern. In section II we present the numerical simulations, including the numerical methods, models and results, numerical accuracy, and particle trajectory simulation. Section III shows experiments in which the test device, micro-PIV setup and the motion of particles obtained from PIV measurement are presented. In section IV, a brief discussion of the results, including a comparison between the numerical simulation and the experimental measurement and the mechanism of the observed streaming pattern, is given and overall conclusions are drawn in section V.

II. Numerical simulation

1. Background – Limiting velocity method.

In this section, a numerical model is introduced to simulate the three dimensional streaming field in our capillary device, described below, using the *limiting velocity method*. This method was first introduced by Nyborg[26] in 1958 and modified by Lee and Wang[27] in 1988. It was shown that if the boundary has a radius of curvature that is large compared to the acoustic viscous boundary layer, then the time averaged velocity at the extremity of the inner streaming (the "limiting velocity") can be approximated as a function of the local, first order linear acoustic field (when solved with the surface replaced by a slip boundary condition). The streaming in the bulk of the fluid can then be predicted by a fluidic model that takes the limiting velocity as a boundary condition. A schematic of the streaming flow over a vibrating surface is shown in Fig. 1.

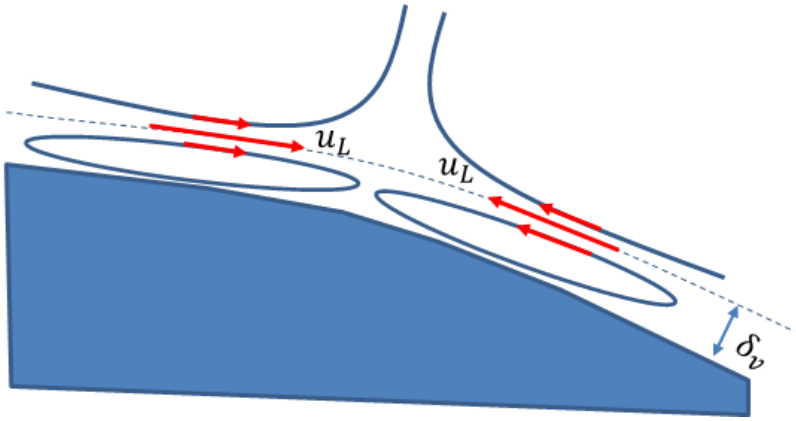

Fig. 1. Schematic of the streaming field over a vibrating surface, where u_L is the limiting velocity and δ_v is the viscous penetration depth.

Thus, this approach only predicts the velocity of the streaming field *outside* the viscous boundary layer, and does not calculate the streaming field inside the acoustic viscous boundary layer. In typical acoustofluidic devices working in the MHz region this is useful as we are generally interested in the main body of the fluid which is typical several orders of magnitude thicker than the acoustic viscous boundary layer which has thickness[28]:

$$\delta_v = \sqrt{\frac{2\nu}{\omega}}, \tag{1}$$

where ν is the kinematic viscosity of the fluid and ω is the angular frequency. At 1 MHz in water this has a value of about 0.6 μm.

This decomposition of the problem (into the steps described below) is only valid if the mass source term in the streaming field described by Muller et al.[29] in their equation (9a) can be ignored. Nyborg[26] justifies this approximation in his derivation of the limiting velocity in the paragraph above his equation (10).

The limiting velocity represents the streaming immediately outside the viscous boundary layer, and has components, u_L and v_L, given by[27]:

$$u_L = -(4\omega)^{-1} Re\left\{q_x + u_1^*\left[(2+i)\nabla\cdot\boldsymbol{u_1} - (2+3i)\frac{\partial w_1}{\partial z} - (2-i)H\, w_1\right]\right\}, \quad (2)$$

$$v_L = -(4\omega)^{-1} Re\left\{q_y + v_1^*\left[(2+i)\nabla\cdot\boldsymbol{u_1} - (2+3i)\frac{\partial w_1}{\partial z} - (2-i)H\, w_1\right]\right\}, \quad (3)$$

where

$$q_x = u_1\left(\frac{\partial u_1^*}{\partial x} + v_1^* T_{121}\right) + v_1\left(\frac{\partial u_1^*}{\partial y} + v_1^* T_{122}\right), \quad (4)$$

$$q_y = u_1\left(\frac{\partial v_1^*}{\partial x} + u_1^* T_{121}\right) + v_1\left(\frac{\partial v_1^*}{\partial y} + u_1^* T_{122}\right), \quad (5)$$

Where u_1, v_1 and w_1 are components of the complex acoustic velocity vector, $\boldsymbol{u_1}$ (the subscript helps distinguish this first order term from the second order streaming velocity, $\boldsymbol{u_2}$, described later). The superscript, $*$, is the complex conjugate. The indices i, j, and k represent the three coordinates x, y and z. T_{ijk} and H are geometric parameters (of units [m^{-1}] and [non-dimensional] respectively) that relate to the curvature and orientation of the surface relative to the coordinate system[27], making this expression general for limiting velocities on all shapes and orientations of boundaries (subject to the constraint that the curvature is small compared to the viscous boundary layer).

On a planar surface that is normal to z, the equations simplify to the following form:

$$u_L = -\frac{1}{4\omega} Re\left\{u_1\frac{du_1^*}{dx} + v_1\frac{du_1^*}{dy} + u_1^*\left[(2+i)\left(\frac{du_1}{dx} + \frac{dv_1}{dy} + \frac{dw_1}{dz}\right) - (2+3i)\frac{dw_1}{dz}\right]\right\}, \quad (6)$$

$$v_L = -\frac{1}{4\omega} Re\left\{u_1\frac{dv_1^*}{dx} + v_1\frac{dv_1^*}{dy} + v_1^*\left[(2+i)\left(\frac{du_1}{dx} + \frac{dv_1}{dy} + \frac{dw_1}{dz}\right) - (2+3i)\frac{dw_1}{dz}\right]\right\}, \quad (7)$$

2. Finite Element Models

The model was implemented in the finite element package COMSOL[30]. The numerical procedure can be split into three steps. First, a linear acoustic model is used to find the first-order resonant acoustic pressure and velocity fields, from which the limiting velocities can be derived. Second, the limiting velocities are found using equations (6)-(7) above, which are functions of the linear acoustic velocities. These are then applied as boundary conditions to a Navier-Stokes creeping flow model to obtain the time averaged fluid motion (the streaming). Finally, a 'particle tracing for fluid flow' model was used to simulate the particle trajectories under the combined action of ARF and ASF.

The model geometry is formed from a cuboidal domain of dimensions $0.3 \times 6 \times 10$ mm^3 (height × width × length). Here, only the fluid layer within a section of the capillary was modelled for the following reasons: (1) without the transducer and glass walls of the capillary, the whole model is computationally simpler. The numerical process, including the simulation of the first-order acoustic field and the acquisition of the acoustic streaming field can be finished in one hour. While it is possible to model the full device, including piezoelectric and fluid-solid couplings, the additional complexity places high demands on workstation memory; (2) This reduced model is shown below to successfully predict the observed phenomena, which demonstrates that the essential physics is already captured by the model, and thus when we discuss the physical origin of this type of streaming pattern we are in a stronger position to identify the mechanism. In the following sections, each step is examined in more detail.

A. Comparison of the approach with classical solutions

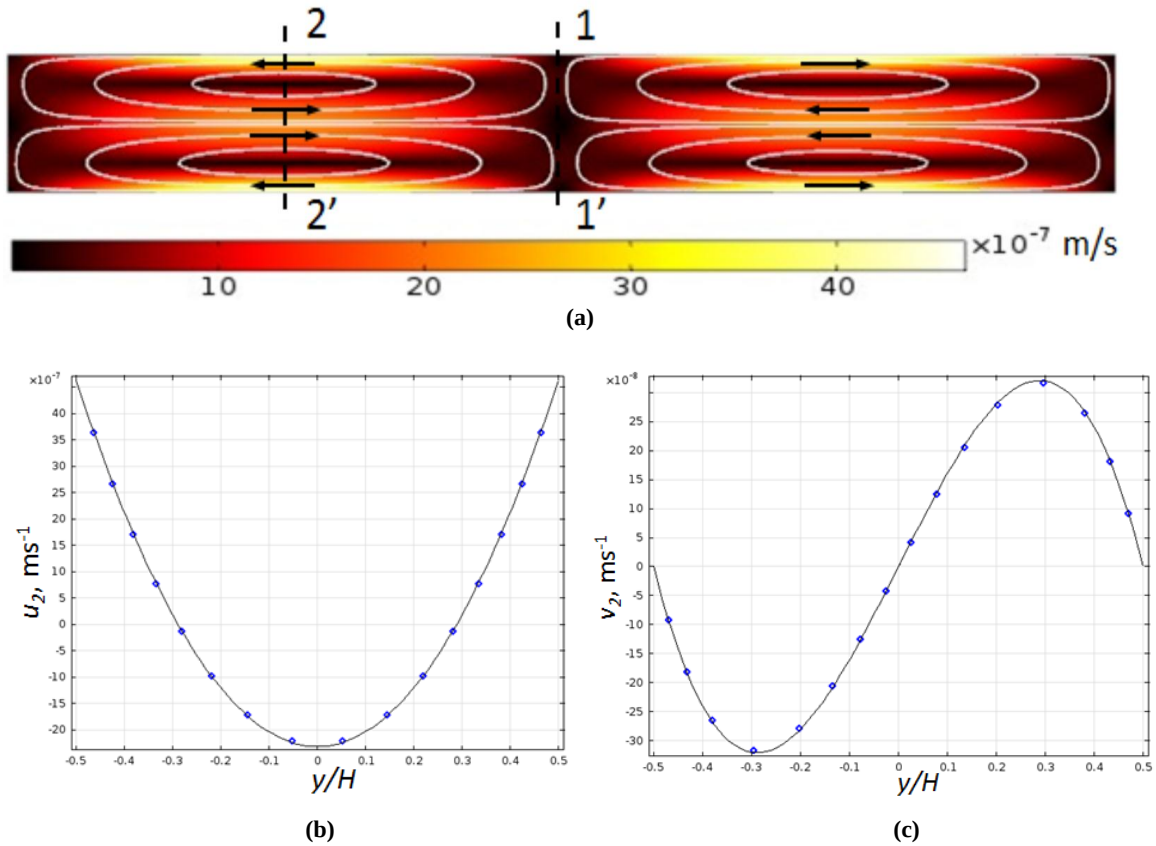

Fig. 2. (a) Modelled Rayleigh streaming in a 2D rectangular chamber (b) u_2, the x-component of streaming velocity, along line 1-1' ($x = -L/4$); (c) v_2, the y-component of streaming velocity, along line 2-2' ($x = 0$). Diamonds show model results and solid lines are the results obtained from Rayleigh's analytical solution.

Firstly, the applicability of this approach to modelling the streaming is ascertained by applying the methodology described above to a 2 dimensional model of a rectangular chamber (Fig. 2 (a)) with an aspect ratio chosen so that classical Rayleigh streaming predominates. The model parameters are summarised in Table 1. The small mesh size is required to accurately resolve the inner streaming vortex. The linear acoustic step has the left wall excited by a sinusoidal pressure fluctuation of amplitude 0.2 MPa, with the remaining boundaries set to be reflecting. In the fluid motion step, the bottom and top walls are set to have limiting velocity boundary conditions (derived from the linear acoustic quantities) and the left and right walls are slip boundaries. It can be seen from Fig. 2 (b),(c) that the model is in good agreement with the classical results of Rayleigh[11].

Table 1 2D Rayleigh streaming model parameters.

Dimension of enclosure (length L X height H):	0.74 mm × 84.8 μm	Driven frequency, f:	1 MHz
Excitation pressure amplitude, p:	0.2 MPa	Dynamic viscosity of water, μ:	8.9×10^{-4} Pa s
Density of water, ρ_p:	1000 kg/m^3	Mesh size:	1 μm

B. First-order acoustic field

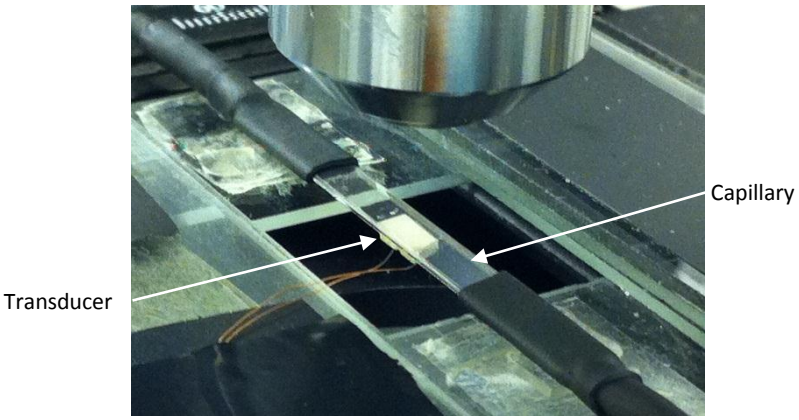

Fig. 3. An example capillary particle manipulation device. This particular device lacks the gold foil electrode, allowing the transducer to be seen.

Having established the viability of the approach by comparison with Rayleigh streaming solutions, the capillary device shown in Fig. 3 was modelled using the COMSOL 'pressure acoustic' option to obtain the first-order acoustic field. This solves the harmonic, linearized acoustic problem, which takes the form[31]:

$$\nabla^2 p = -\frac{\omega^2}{c^2}\, p \tag{8}$$

where p is the complex pressure defined at position r using the relation,

$$p_t(r,t) = Re\{\, p(r) e^{-j\omega t}\,\} \tag{9}$$

and makes the assumptions[31] of small acoustic disturbances, an inviscid and Newtonian fluid, and adiabatic processes. The fluid is also assumed at rest so the streaming velocities must be small in comparison to acoustic velocities. It can be seen in the following that all of these approximations are upheld in the device presented here.

The bottom surface was given a normal-acceleration boundary condition, the left and right walls were considered as plane wave radiation boundary conditions (to represent energy that travels down the capillary being largely absorbed by the tubing and connectors at the ends), and the remaining side walls and roof were hard boundary conditions. The standing wave field within the fluid layer was generated by a sinusoidal acceleration of the bottom wall. A 2D normal distribution is used to represent the reduction in vibration amplitude away from the transducer area:

$$a_n = a_0 e^{-ax^2 - by^2}. \tag{10}$$

To assess the validity of this approach, the vibration profile was compared with a full model (composed of transducer and glass capillary), which shows that similar acoustic acceleration and velocity distributions on the bottom surface were obtained from these two models. Then, five sets of 'a' and 'b' coefficients (respectively, with units m^{-2}, $a=0.22\times10^6$, $b=0.22\times10^6$; $a=0.22\times10^6$, $b=5\times10^5$; $a=0.22\times10^6$,$b=2\times10^6$; $a=5\times10^5$, $b=5\times10^5$; $a=5\times10^5$,$b=2\times10^6$) in the above equation were examined, to represent the area of the excitation from the transducer. It was found that the streaming field was similar from all excitations, suggesting that the streaming pattern is reasonably robust to the precise choice of the excitation shape. This approach is similar to that described by Muller *et al.*[29] who represented ultrasonic actuation with a velocity boundary condition when simulating the Rayleigh streaming in a 2D rectangular chamber. The results presented in this paper are for an excitation of $a=5\times10^5$ and $b=2\times10^6$ m^{-2}.

The frequency of the half-wave resonance was found at 2.479 MHz by using a parametric sweep to plot the average acoustic energy density in the fluid layer versus driving frequency. This method has been found to be more reliable than sorting through the very large number of modes presented by a modal analysis. The simulated acoustic pressure field is shown in Fig. 4. Fig. 4 (a) represents the magnitude of the acoustic pressure on the surfaces of the chamber and Fig. 4 (b) the magnitude along the centre line ($x = 0,\ y = 0, -H/2 \le z \le H/2$).

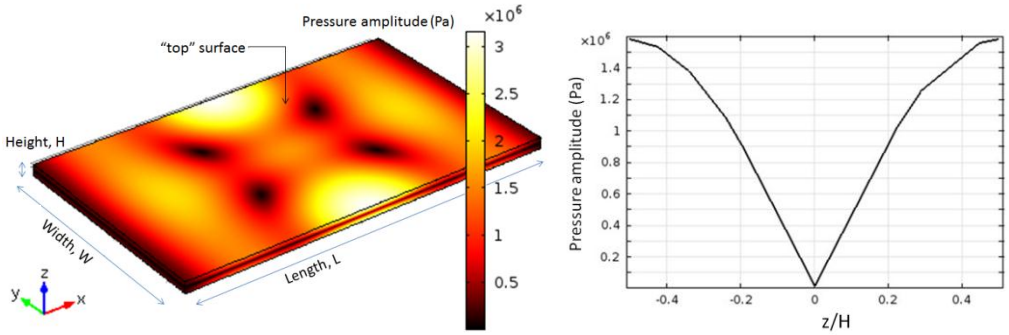

(a) (b)

Fig. 4. (a) Magnitude of the acoustic pressure in the fluid layer at the surfaces of the modelled volume; (b) acoustic pressure amplitude distribution at the centre line ($x = 0,\ y = 0, -H/2 \le z \le H/2$)

C. Acoustic streaming field

The COMSOL 'creeping flow' model was used to simulate the acoustic streaming field. This approximates the fluid as incompressible, and neglects inertial terms (Stokes flow) as the Reynolds number is much smaller than one in the experiments presented in this paper. In the body of the fluid the governing equations for the streaming velocity field, $\boldsymbol{u_2}$, and associated pressure field, p_2, are

$$\nabla p_2 = \mu \nabla^2 \boldsymbol{u_2} \tag{11a}$$

$$\nabla . \boldsymbol{u_2} = 0 \tag{11b}$$

The bottom and top walls were considered as limiting velocity boundary conditions while the remaining four walls were considered as slip boundary conditions. Initial modelling had represented the side walls (at y=±3 mm) as limiting velocity boundary conditions and the resulting pattern was a combination of classical Rayleigh streaming in the vicinity of the side walls superimposed on the larger scale transducer-plane streaming. However, to aid clearer presentation of the results we limit ourselves in this paper to presenting the transducer-plane streaming generated by the limiting velocities of the floor and ceiling of the device and neglect the localised Rayleigh streaming generated by the side walls.

In order to investigate the effects of mesh size on the modelled results, a mesh dependency study of the 3D model is presented here. A series of tetrahedral meshes with size ranging from 0.03 mm to 0.17 mm was simulated. The average value of the magnitude of streaming velocity in the whole device, $\bar{u}$, for each case was obtained. The normalised average streaming speed $\bar{u}/\bar{u}_{ref}$ where $\bar{u}_{ref}$ is the average streaming speed for a mesh size of 30 μm is plotted in Fig. 5. It can be seen clearly that, with the decrease of mesh size corresponding to a finer mesh, the modelled streaming speed becomes larger and approaches a steady value. In order to balance the computer efficiency and the accuracy of simulation, a tetrahedral mesh of size 0.06mm was used for the remainder of results presented in this paper, resulting in an estimated mesh-induced numerical error of 0.7%.

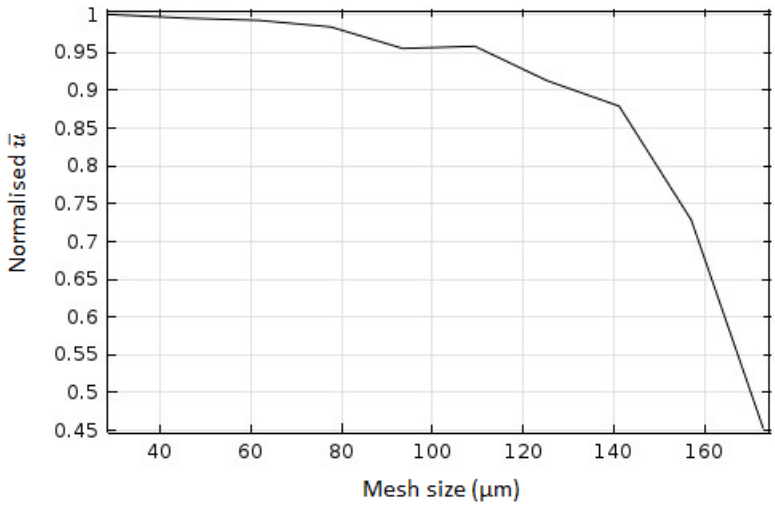

Fig. 5. Relationship between the average streaming speed $\bar{u}$ and mesh size

Fig. 6 shows the modelled 3D fluid motion within the fluid layer. It can be seen clearly that four quadrant streaming vortices, symmetric to the centre of the device, are obtained. Fig. 6 (c)-(d) shows the streaming velocity magnitude through cross-sections in the *yz* plane 1-1' and 2-2', shown in Fig. 6 (b). From Fig. 6 (a) and (b), we can see that the predominant motion is in-plane and that at the centre of the device, all the velocity vectors run parallel to each other.

Table 2 3D Model parameters.

Domain size (length, L, x Width, W, x height, H.):	10 mm x 6 mm x 0.8 mm	Excitation frequency, f:	2.479 MHz
Mesh size:	60µm, tetrahedral	Dynamic viscosity of water, μ:	8.9×10^{-4} Pa s
Density of water, ρ_p:	1000 kg/m^3	Speed of sound, water:	1481.4 m s^{-1}
Excitation: Peak normal acceleration :	3.2 x 10^5 m s^{-2}		

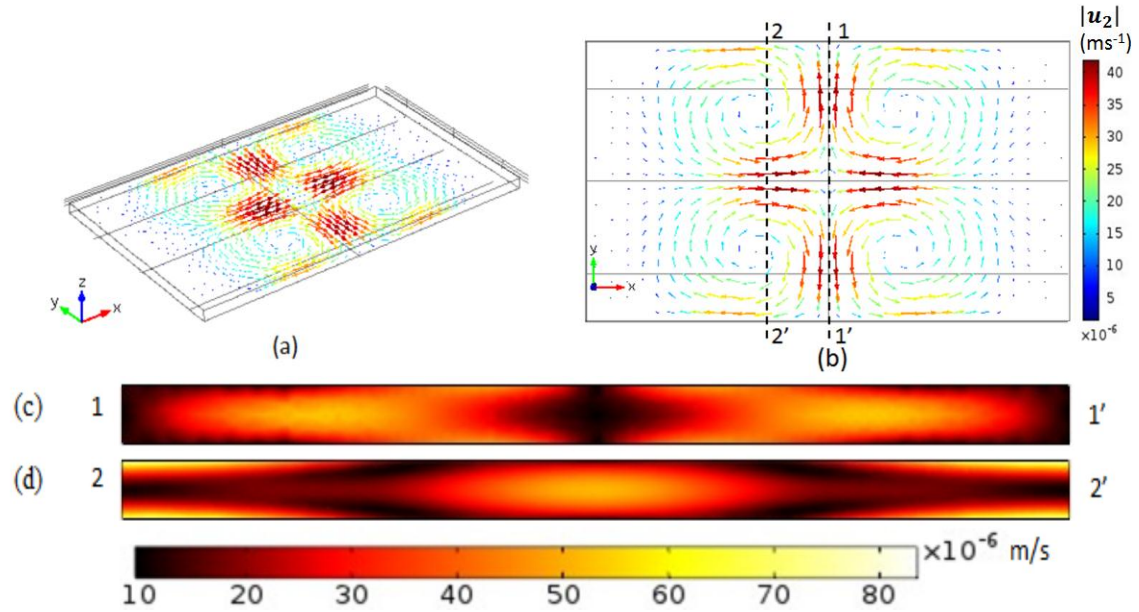

Fig. 6. Acoustic streaming velocity field, $\boldsymbol{u_2}$: (a,b) The modelled 3D fluid motion, velocity vectors are shown at two heights within the chamber (z-positions of one third and two thirds of the chamber height); (c,d) streaming velocity magnitude on cross-sections 1-1' and 2-2' (not to scale: z dimension has been stretched for clarity)

To establish that truncating the length of the capillary that is modelled does not have a significant effect on the results (ie investigating whether those regions at some distance from the transducer contribute significantly to the streaming) we considered a range of different values of the capillary lengths: 8, 10, 16 and 18 mm. It was found that at 8 mm (when the length is comparable to the width) the truncation had significant effect on the acoustic field, and actually caused streaming vortices with rotation in the opposite direction to the other cases. The remaining lengths produced similar results, with an error in the maximum velocity of no more than 6 %. The remaining results in this paper are for a length of 10 mm unless otherwise stated.

Due to the quadratic dependence of the limiting velocity on the linear acoustic quantities, the relationship between the maximum streaming velocity in the device u_{2max} and the maximum acoustic pressure, p_{max}, was expected to take the form

$$u_{2max} = \alpha\, p_{max}^2, \tag{12}$$

where α is a constant. This was tested by applying to a range of excitation amplitudes to the transducer. The quadratic dependence was valid, and the constant, α, was found to take the value 47.23 m s^{-1} MPa^{-2} for the stated dimensions. This relationship is discussed further in comparison with experimental results in Fig. 10 below.

D. Particle trajectories

In order to understand the effects of acoustic streaming on particle manipulation, a numerical simulation of particle trajectories is presented here. Neglecting the gravity force and buoyancy force on a spherical particle, the movement of the particle within a standing wave field is determined by the acoustic radiation force[32], F_{ac}, and streaming drag force, F_d:

$$\frac{d}{dt}(m_p v) = F_d + F_{ac}, \tag{13}$$

$$F_{ac} = -\nabla\left(V_0\left(\frac{3(\rho_p - \rho_f)}{2\rho_p + \rho_f}\overline{E_{kin}} - \left(1 - \frac{\beta_p}{\beta_f}\right)\overline{E_{pot}}\right)\right), \tag{14}$$

$$F_d = 6\mu\pi r(u - v), \tag{15}$$

where m_p is the particle mass, v is the velocity of the particle, u is the fluid velocity, μ is the fluid viscosity, r is the particle radius, $\overline{E_{kin}}$ and $\overline{E_{pot}}$ are the time average kinematic and potential energy, ρ_p and ρ_f are respectively the density of particle and fluid, β_p and β_f are the compressibility of particle and fluid, and V_0 is the particle volume. Equation 14 is correct for the gradient forces found in both standing waves and in travelling wave fields with energy density gradients (e.g. valid in travelling waves in the near field and in Bessel beams). In the absence of gradient forces an additional, order of magnitude smaller[7], contribution from pure scattering become important; however, this will be small here compared to the gradient forces.

From this theory, together with the two models introduced in Sections B and C above, a COMSOL 'Particle Tracing for Fluid Flow' model was used to simulate the particle trajectories. The shape of the trajectories are independent of the pressure amplitude, since both the radiation forces and induced drag forces scale with the square of pressure; results are presented here for an excitation amplitude of a_0=3.2$\times 10^5$ m s^{-2}. An array of tracer particles (given the properties of polystyrene beads of diameter 1 µm) are seeded at time $t = 0$. Both acoustic radiation forces and streaming drag forces act on the particles, resulting in the motion shown in Fig. 7. The quadrant vortex pattern symmetric to the centre of the device is clearly seen, matching that observed in the experimental visualisation. The predominant acoustic radiation forces act perpendicular to the transducer to push the beads towards the nodal plane. It can be seen that over the course of a single rotation the lateral acoustic radiation forces (acting parallel to the transducer) are small in comparison to the forces causing the rotational motion.

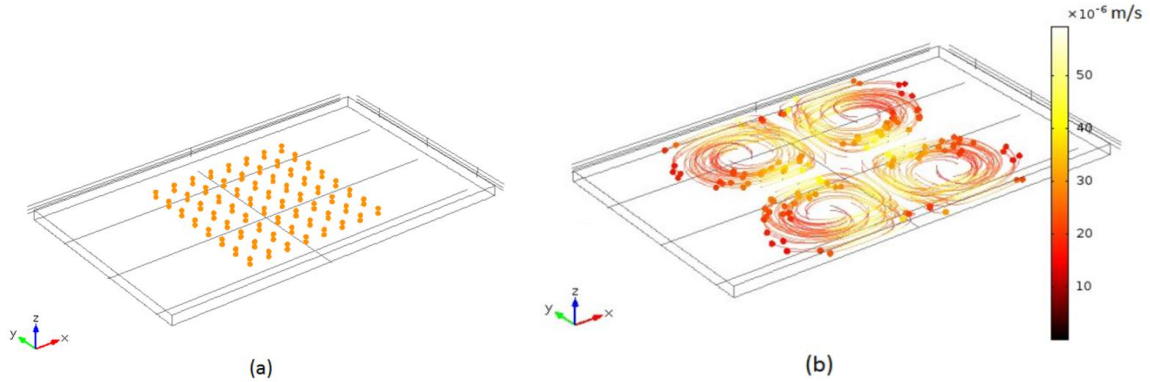

Fig. 7. Three-dimensional view of modelled particle trajectories: spheres represent 1 µm beads (initially arranged in an 10×8×2 array) with lines showing their corresponding trajectories. Colour shows velocity according to legend. A full animation of this simulation can be seen in the Electronic Supplementary Information.

III. Experimental

1. Test Device

The test device was composed of a PZT4A transducer (Ferroperm, 3 mm × 3 mm × 1 mm thick) glued to a glass capillary of approximately rectangular cross-section, as shown in Fig. 8. The glass capillary (Vitricom) had inner dimensions of 0.3 mm × 6 mm, wall thickness of 0.3 mm, and length 50 mm. To make the top electrode connection a sheet of gold foil was placed between the transducer and the capillary (glues: epoxy, epotek 301 between capillary and leaf, and Circuitworks silver loaded epoxy between leaf and transducer, measured glue layer thicknesses <10 µm). Soldered connections were made between the gold leaf, top electrode and connecting wires. Fluidic connections were made to the capillary via PTFE tubing (ID 1 mm) attached via heat-shrink sleeving. The advantage of a capillary device such as this is that, in contrast to many other layered resonators, there is little energy dissipated into support and clamping structures which makes the modelling of the device more straightforward.

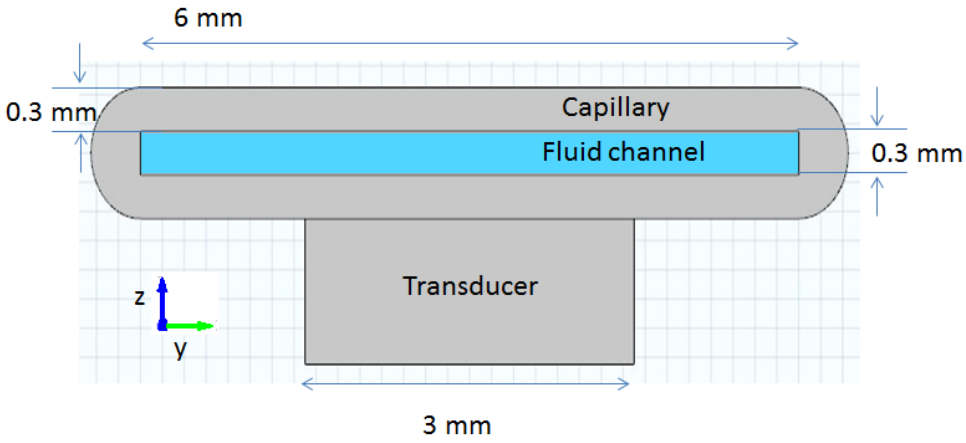

Fig. 8. Cross-section of the device

2. PIV setup

Measurements of the acoustic streaming field were performed using the experimental arrangement shown in Fig. 3. A function generator (TTi, TG1304 Programmable) drives an RF amplifier (EIN, Model 240L) that drives the transducer, with signal monitored by an oscilloscope (Agilent Technologies, DOS1102B Digital Storage Oscilloscope). An Olympus BXFM epi-fluorescent microscope with a *pixelfly* dual-frame CCD camera was used to image the device.

Impedance measurements were used to identify the half-wave resonance frequency (corresponding to a half wavelength within the fluid layer of the capillary in the *z* direction), at 2.585 MHz. At this frequency it was observed that if 10 µm polystyrene beads were introduced they were both levitated in the *z*-direction, and more slowly agglomerated into a clump above the centre of the transducer. This relates to radiation forces arising from gradients in predominantly the potential and kinetic energy densities respectively as discussed by Glynne-Jones *et al.*[25, 33]. For beads of this size streaming effects were not in evidence due to the much larger radiation forces. While temperature effects are known to have an influence on the resonances in devices such as this[34], the streaming pattern was found to be reliably present at this frequency and the streaming magnitude similar and within the level of accuracy resulting from the approximations made in the modelling below.

PIV measurements were performed using green-fluorescent 1 µm polystyrene tracer beads (Fluoresbrite microspheres, Polysciences Inc.). While these experience small radiation forces toward the nodal plane, the streaming forces are found to be a factor of around 4 stronger. Experiments were conducted with a fresh fill of beads for each measurement to ensure a homogeneous bead distribution. Image pairs were captured at measured intervals of about 280 ms and processed using the *Matlab* based Micro-particle-image-velocimetry (µPIV) software, *mpiv*[35].

3. Observed Streaming Patterns

A four quadrant, steady acoustic streaming pattern symmetric to the centre of the device was formed, shown in Fig. 9. The plane of these vortices is parallel to the transducer plane (i.e. perpendicular to axis of the standing wave). This is in contrast to the rolls often observed as a result of Rayleigh streaming[11], which have components parallel to the sidewall of chambers.

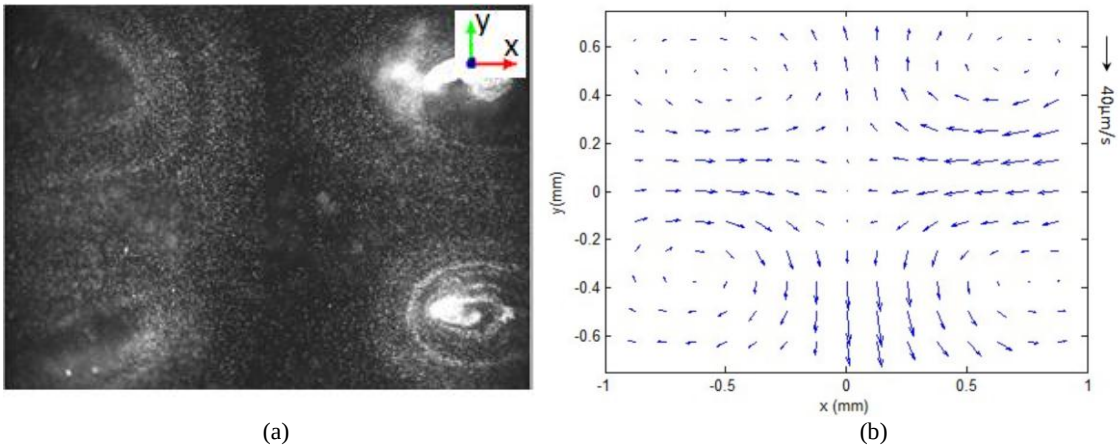

(a) (b)

Fig. 9. (a) A photographic image of distribution of beads in the fluid after some minutes of streaming. Beads can be seen to have agglomerated near the centre of the streaming vortices; (b) PIV measurements of acoustic streaming (measurements taken after a fresh population of beads have been flowed in to ensure an even distribution). The field of view is smaller than the transducer area. A video of this behaviour can be seen in the Electronic Supplementary Information.

A. Acoustic pressure measurement

The acoustic pressure amplitude in the device was measured using the 'voltage drop' method described by Spengler *et al.*[23]. In static equilibrium a particle in an ultrasonic force-field will settle to a position where the gravitational and buoyancy forces balance with the acoustic forces. Like the acoustic radiation force, gravitational and buoyancy forces are both proportional to particle volume, so the equilibrium position is independent of particle size. A test particle is placed in the field; as the acoustic field is decreased the particle equilibrium position sinks, until it reaches the turning point of the radiation force vs position graph, where further decrease leads to the particle dropping. Since the material properties and hence buoyancy force on the particle are known, the acoustic energy density and hence pressure amplitude can be calculated.

Table 3 shows the material properties used in the experiment. The 'drop voltage', was determined by viewing a 10 μm diameter polystyrene bead with a 50x microscope objective. The system can be approximated as linear since $|p|<<(\rho c^2$=2.2 GPa), so the pressure magnitude is proportional to the driving voltage, and therefore the acoustic radiation force is proportional to the square of the applied voltage.

Thus, the pressure amplitude above the transducer at voltage, V_{in}, was calculated to be given by

$$|p| = \sqrt{\frac{F_{ac}\rho_f c_f^2}{\pi k r^3 \varphi(\rho,\beta)}} \cdot \frac{V_{in}}{V_d}, \tag{16}$$

where all the variables are defined and summarised in Table 3, except $\varphi(\rho,\beta)$, which, is often known as acoustic contrast factor and can be calculated from

$$\varphi(\rho,\beta) = \frac{\rho_p + \frac{2}{3}(\rho_p - \rho_f)}{2\rho_p + \rho_f} - \frac{\beta_p}{3\beta_f}, \tag{17}$$

where β, the compressibility is equal to $1/\rho c^2$.

B. Effects of driving voltage on acoustic streaming

The effects of driving voltage on the streaming pattern and magnitude of the streaming velocities were investigated. A series of excitation voltages, ranging from 10 V to 30 V, was considered. For each condition the streaming field was measured. The large margin of error on this measurement is due to a number of factors: (a) the difficulty of measuring the 'drop voltage' precisely due to uncertainty in knowing when equilibrium has been passed (b) uncertainties in the material properties of the bead. To compare the different cases, the maximum streaming velocity (found close to the position x=1 mm, y=0, in Fig. 9) had been plotted against maximum pressure amplitude, which will be discussed in comparison to the numerical modelling in section IV.

Table 3. Acoustic pressure measurement

Driving frequency, f: 2.585 MHz	Particle radius, r: 5 μm
Particle density, ρ_p: 1055 kg/m^3	Fluid density, ρ_f: 1000 kg/m^3
Acoustic speed in particle, c_p: 1962 m/s	Acoustic speed in fluid, c_f: 1480 m/s
Acoustic pressure amplitude, $\|p\|$: $(2.685\times10^4 \times V_d)$ Pa	Energy density, ε: $(0.082 \times V_d^2)$ J/m^3
Drop voltage, V_d: 1.08 V	

IV. Discussion

1. Comparison between experiment and model

The acoustic streaming field within the transducer-capillary device has been investigated using both experimental and numerical approaches. It can be seen from Fig. 9 that the modelled four-quadrant streaming pattern, symmetric to the centre of the device and parallel to the transducer plane, is in good agreement with the visualised streaming pattern in experiments. The magnitude of streaming velocity obtained from simulation also compares well with the experimental measurement, shown Fig. 10.

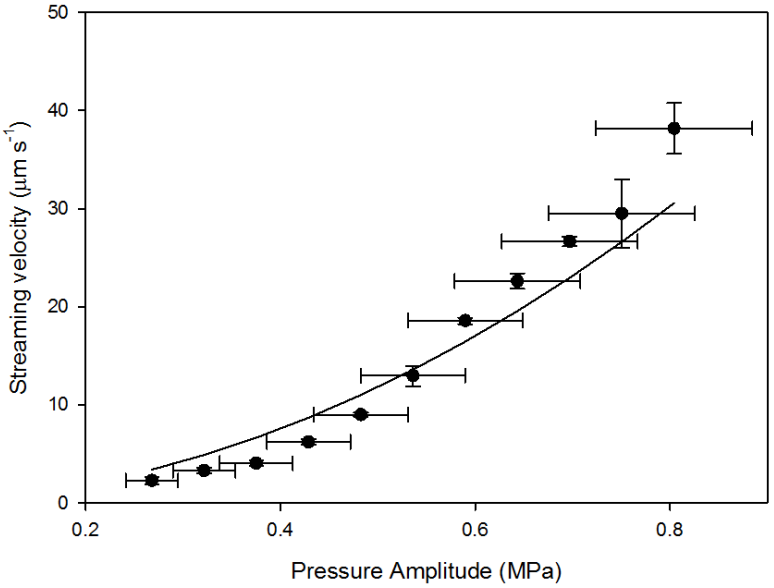

Fig. 10. Relationship between the magnitude of maximum streaming velocity and driven acoustic pressure, a comparison between PIV measurement and numerical simulation, where the line and points show respectively the simulated and measured results.

The differences between the modelled streaming velocity and the measured value may be attributed to the reasons listed below:

1. Acoustic pressure measurement. As described above, the voltage-drop method of pressure measurement is subject to significant errors. Other methods involving PIV based bead tracking[4] have been shown much more accurate, although this method would be hard to apply in this case due to the radiation force being in line with the viewing direction.
2. The model is a simplification, neglecting coupled resonances that include the transducer and glass walls. Hence the modelled resonance is at a slightly different frequency to that found experimental (2.585MHz Measured vs 2.479MHz modelled).
3. The temperature of the device has not been stabilised. Experiments[4] have shown that self-heating of the transducer and attached structures at higher drive levels can cause a shift in the resonant frequency of the system. We hypothesise that this is the cause for the small steepening of the experimental results with frequency (ie the curve is steeper than a quadratic one). Temperature stabilisation in this system is not straightforward (compared to the silicon devices presented by Augustsson *et al.* [4]) as the air boundaries of the device are an integral part of the design, and do not allow for thermal connections.
4. Bruus *et al.*[21] have recently modelled Rayleigh streaming in a glass capillary to a higher level of precision. They show that including thermo-viscous effects, not modelled here, produces a significant correction in systems such as these.
5. The capillary chamber is not perfectly rectangular in cross-section, which will influence the acoustic resonance and resulting streaming pattern.

However, despite these approximations and uncertainties, the model and experiments are sufficient to both demonstrate the existence of the transducer-plane streaming patterns, and also deduce the causal mechanism as discussed next.

2. Mechanism of the in-plane streaming pattern

Equations (6)-(7) for the limiting velocity have a number of terms that are functions of the acoustic velocity components and their derivatives. Numerically examining the limiting velocities on the $z = -H/2$ and $z = H/2$ boundaries (those primarily driving the observed pattern), we find that they are dominated by the term which is the product of the acoustic velocity parallel to the surface and the z-gradient of acoustic velocity in the z-direction, du_z/dz. This reflects the strong axial velocity gradients found in planar manipulation devices ($du/dx \ll dw/dz$ and $dv/dy \ll dw/dz$). For example, the x-component limiting velocity u_L is approximated by the term,

$$u_L \approx -\frac{1}{4\omega} Re[\,-2i\, u_1^* \frac{dw_1}{dz}] \tag{18}$$

where the superscript, $*$, shows the conjugate value of the complex acoustic velocity. To find the meaning of the term, $u_1^* dw_1/dz$, we consider the linearized equation of mass conservation,

$$\rho_0 \nabla \cdot \boldsymbol{u_1} = -\frac{\partial \rho}{\partial t}. \tag{19}$$

In planar manipulation devices the gradients of the velocity in the z-direction are much greater than in the lateral directions due to the planar geometry[36], hence the left side of equation (19) can be approximated as

$$\rho_0 \frac{dw_1}{dz}. \tag{20}$$

Meanwhile, using standard relations between density and pressure in linear acoustics[31] and then exploiting the harmonic nature of the excitation, the right hand side of equation (19) becomes

$$-\frac{\partial \rho}{\partial t} = -\frac{1}{c^2}\frac{\partial p}{\partial t} = \frac{1}{c^2}(i\omega p). \tag{21}$$

Thus, equation (19) can be written

$$\frac{dw_1}{dz} \approx \frac{1}{\rho_0 c^2}(i\omega p). \tag{22}$$

Using this, the product $u_1^* dw_1/dz$ can be approximated as

$$u_1^* \frac{dw_1}{dz} \approx u_1^* \left(\frac{i\omega p}{\rho_0 c^2}\right) = \frac{i\omega}{\rho_0 c^2}(u_1^* p) = \frac{i\omega}{\rho_0 c^2} 2\, C_x. \tag{23}$$

where the complex intensity, C_x, is given by:[37]

$$C_x = \frac{1}{2} u_1^* p \tag{24}$$

Thus the *x* component of the limiting velocity can be written

$$u_L \approx \frac{-1}{\rho_0 c^2} Re[C_x]$$

$$\text{valid for } du/dx \ll dw/dz \text{ and } dv/dy \ll dw/dz \tag{25}$$

According to Fahy[37], the complex intensity (a harmonic representation of the real, instantaneous intensity, which is a function of time) can be decomposed into two parts: (i) the real part, called the active intensity, which gives the time average energy flow; and (ii) the imaginary part (the reactive intensity) which corresponds to local, oscillatory energy flows with zero time average. We see from equation 25 that the limiting velocity is proportional to the active intensity. Fahy shows that the active intensity can have a rotational component in fields that have a standing wave component (and that the reactive intensity is irrotational). He states that in standing wave fields this rotation should be interpreted as reflecting the elliptical path of fluid elements rather than a larger scale circulation of energy. The active acoustic intensity vector at the bottom boundary is plotted in Fig. 11. It can be seen clearly that the pattern it forms is closely related to the modelled and observed streaming patterns. The insight that these streaming patterns are thus caused, may lead in the future to better control, or elimination of the streaming through more careful control of the interplay between standing and travelling waves in the lateral extents of devices.

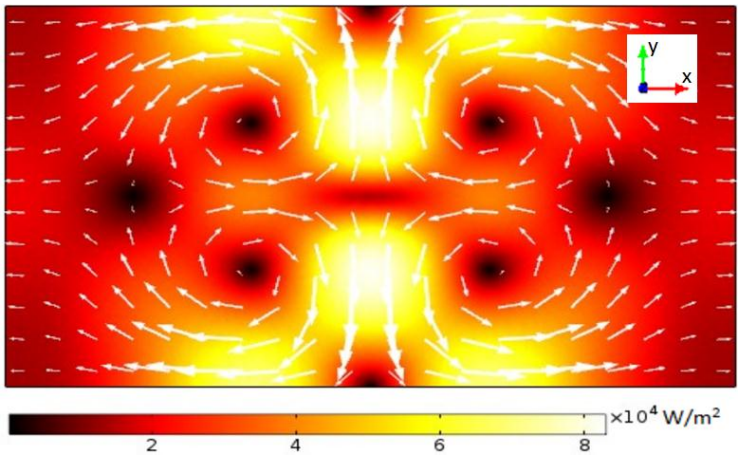

Fig. 11. Active acoustic intensity field at the bottom wall (limiting velocity boundary)

V. Conclusions

A four-quadrant acoustic streaming pattern, symmetric to the centre of the transducer and with the circulation plane parallel to the transducer plane, was experimentally visualised in our planar cell manipulation devices. This kind of acoustic streaming pattern is different from the better-known Rayleigh and Eckart type pattern, both in the shape of streaming flows it generates and in its genesis. The pattern described by Coakley *et al.* in 2004 has not previously been explained; we have presented for the first time an investigation into its mechanism, and have shown that the streaming pattern is related to the active acoustic intensity, which is known to show rotation in a standing wave field.

Experimental work with tracer beads and micro-PIV has quantified the streaming flows for a range of excitations. It has been found to show good agreement with a finite element model that decomposes the streaming problem into three steps, using results from a linear acoustic analysis to calculate limiting velocities that are applied as boundary conditions to a Stokes flow model.

VI. Acknowledgement

The authors gratefully acknowledge the financial support for this work received from China Scholarship Council (CSC) and the EPSRC under the Sonotweezers project (EP/G012075/1)

References

1. J. Friend and L. Y. Yeo, *Rev Mod Phys*, 2011, **83**, 647-704.
2. H. Bruus, J. Dual, J. Hawkes, M. Hill, T. Laurell, J. Nilsson, S. Radel, S. Sadhal and M. Wiklund, *Lab Chip*, 2011, **11**, 3579-3580.
3. R. Barnkob, P. Augustsson, T. Laurell and H. Bruus, *Lab Chip*, 2010, **10**, 563-570.
4. P. Augustsson, R. Barnkob, S. T. Wereley, H. Bruus and T. Laurell, *Lab Chip*, 2011, **11**, 4152-4164.
5. R. Barnkob, I. Iranmanesh, M. Wiklund and H. Bruus, *Lab on a Chip*, 2012, **12**, 2337-2344.
6. K. Yosioka and Y. Kawasima, *Acustica*, 1955, **5**, 167-173.
7. L. P. Gor'kov, *Sov. Phys. Dokl.*, 1962, **6**, 773-775.
8. J. F. Spengler, W. T. Coakley and K. T. Christensen, *Aiche Journal*, 2003, **49**, 2773-2782.
9. L. A. Kuznetsova and W. T. Coakley, *Journal of the Acoustical Society of America*, 2004, **116**, 1956-1966.
10. J. Lighthill, *Journal of Sound and Vibration*, 1978, **61**, 391-418.
11. Lord Rayleigh, *Philosophical Transactions*, 1884, **175**, 1-21.
12. P. J. Westervelt, *J. Acoust. Soc. Am.*, 1952, **25**, 60-67.
13. W. L. Nyborg, *J. Acoust. Soc. Am.*, 1953, **25**, 68-75.
14. H. Schlichting, *Physikalische Zeitschrift*, 1932, **33**, 327-335.
15. S. Boluriaan and P. J. Morris, *Aeroacoustics*, 2003, **2 (3&4)**, 255-292.
16. M. Wiklund, R. Green and M. Ohlin, *Lab on a Chip*, 2012, **12**, 2438-2451.
17. M. F. Hamilton, Y. A. Ilinskii and E. A. Zabolotskaya, *Journal of the Acoustical Society of America*, 2003, **113**, 153-160.
18. M. Kawahashi and M. Arakawa, *Jsme International Journal Series B-Fluids and Thermal Engineering*, 1996, **39**, 280-286.

19. M. K. Aktas and B. Farouk, *Journal of the Acoustical Society of America*, 2004, **116**, 2822-2831.
20. D. Sastrapradja and V. W. Sparrow, *Innovations in Nonlinear Acoustics*, 2006, **838**, 465-468.
21. P. B. Muller, R. Barnkob, M. J. H. Jensen and H. Bruus, *Lab Chip*, 2012, **12**, 4617-4627.
22. B. Hammarstrom, T. Laurell and J. Nilsson, *Lab on a Chip*, 2012, **12**, 4296-4304.
23. J. F. Spengler, M. Jekel, K. T. Christensen, R. J. Adrian, J. J. Hawkes and W. T. Coakley, *Bioseparation*, 2001, **9**, 329-341.
24. C. Eckart, *Phys. Rev.*, 1947, **73**, 68-76.
25. P. Glynne-Jones, C. E. M. Demore, C. W. Ye, Y. Q. Qiu, S. Cochran and M. Hill, *IEEE T Ultrason Ferr*, 2012, **59**, 1258-1266.
26. W. L. Nyborg, *J. Acoust. Soc. Am.*, 1958, **30**, 329-339.
27. C. P. Lee and T. G. Wang, *J. Acoust. Soc. Am.*, 1989, **85**, 1081-1088.
28. H. Bruus, *Lab on a Chip*, 2012, **12**, 1578-1586.
29. P. B. Muller, R. Barnkob, M. J. H. Jensen and H. Bruus, *Lab on a Chip*, 2012, **12**, 4617-4627.
30. Comsol Multiphysics 4.3, http://www.comsol.com/.
31. L. E. Kinsler, A. R. Frey, A. B. Coppens and J. V. Saunders, *Fundamentals of acoustics*, Wiley, New York, 2000.
32. L. P. Gor'kov, *Sov. Phys. Dokl.*, 1962, **6**, 773-775.
33. P. Glynne-Jones, R. J. Boltryk and M. Hill, *Lab on a Chip*, 2012, **12**, 1417-1426.
34. P. Augustsson, R. Barnkob, S. T. Wereley, H. Bruus and T. Laurell, *Lab on a Chip*, 2011, **11**, 4152-4164.
35. N. Mori and C. K-A, mpiv - MATLAB PIV Toolbox, http://www.oceanwave.jp/softwares/mpiv/.
36. P. Glynne-Jones, R. J. Boltryk and M. Hill, *Lab on a Chip*, 2012, **12**, 1417-1426.
37. F.J.Fahy, *Sound intensity*, E & FN Spon, London, 1995.